*Article*

# Wave–Induced Soil Dynamics and Shear Failure Potential around a Sandbar

Ning Chen [1,2], Linlong Tong [1,2,]*, Jisheng Zhang [1,2,]*, Yakun Guo [3,4], Bo Liu [5] and Zhipeng Zhou [5]

1   Key Laboratory of Ministry of Education for Coastal Disaster and Protection, Hohai University,
    Nanjing 210024, China
2   College of Harbor, Coastal and Offshore Engineering, Hohai University, Nanjing 210024, China
3   College of Civil Engineering, Qingdao University of Technology, Qingdao 266033, China
4   Faculty of Engineering and Digital Technologies, University of Bradford, Bradford BD7 1DP, UK
5   China Power Engineering Consulting Group Co., Ltd., Beijing 100032, China
*   Correspondence: tllnj@hhu.edu.cn (L.T.); jszhang@hhu.edu.cn (J.Z.)

**Abstract:** Sandbars are commonly encountered in coastal environments, acting as natural protections during storm events. However, the sandbar response to waves and possible shear failure is poorly understood. In this research, a two–dimensional numerical model is settled to simulate the wave-induced sandbar soil dynamics and instability mechanism. The model, which is based upon the Reynolds-averaged Navier–Stokes (RANS) equations and Biot's consolidation theory, is validated using available experiments. Parametric studies are then conducted to appraise the impact of the wave parameters and soil properties on soil dynamics. Results indicate that the vertical distribution of the maximum vertical effective stress in the sandbar is different from that in the flat seabed, which decreases rapidly along the soil depth and then increases gradually. The impact of soil permeability and saturation on the vertical effective stress distribution around the sandbar also differ from that in the flat seabed. Unlike the flat seabed, the vertical distribution of shear stress in the sandbar increases with an increasing wave period. The sandbar soil shear failure potential is discussed based upon the Mohr–Coulomb criterion. Results show that the range of shear failure around the sandbar is wider and the depth is deeper when the wave trough arrives.

**Keywords:** soil consolidation theory; wave shoaling; shear failure potential; sandbar

## 1. Introduction

Ocean warming caused by global warming is altering the global wave climate and making waves stronger [1]. The maximum wave height and impact area associated with tropical cyclones have increased about 3%/decade and 6%/decade, respectively [2]. During the storm season, the upper part of the beach is eroded and sediment is transported to the offshore area to accumulate, forming a typical sandbar profile [3]. Such sandbars can protect the coast by reflecting landward waves into the ocean [4]. However, the sandbar is unstable under wave loading [5]. The failure of the seabed around the sandbar can be caused by the viscous stresses at the bed surface [6–8], the pore water pressure gradients [9–12], or the effective stresses [13–16]. The instability of the sandbars may cause the evolution of the beach or significant damage to marine structures.

Numerous studies have been undertaken to explore the hydrodynamic characteristics around the coastal sandbars in the past decades. King and Williams [17] made a range of experiments and found that the sand transport reached the maximum at the breaking point, and the sand transport rate increased with increasing wave height. They also found that the wave steepness determined the direction of sand movement. A steep wave moved the sand seawards while a flat wave drove the sand landwards. Benjamin et al. [18] conducted laboratory experiments and found that evolving sandbars might interact with the surface wavefield and enhance wave reflection. Reniers et al. [19] indicated that sandbars enhance

depth–induced wave breaking and observed strong cross–shore flow in the lower part of the water when the waves are broken. Cohn et al. [20] discussed the variation of nearshore hydrodynamics under different multi–bar configurations with XBeach. They indicated that when the wave conditions are consistent, the vertical extent of infragravity runup could vary by up to 36% with different shapes and positions of the sandbars. Chiapponi et al. [21] measured the velocity field produced by regular waves passing a fixed bar and calculated the terms in the vorticity balance equation. Van der A et al. [22] found a strong undertaking on the shoreward side of the fixed bar through a large–scale wave flume experiment. The presence of a fixed sandbar might reduce local turbulence dissipation and increase production in the water column. Van der Zander et al. [23] found that the seaward turbulent kinetic energy transport existed in wave–breaking regions around the sandbar affected by undertow and long–wave velocities. It took several wave cycles to decay the turbulence generated by wave breaking. Mulligan et al. [24] employed a non–hydrostatic wave model to investigate the impact of oblique sandbar morphology on nearshore energy distribution and wave transformation. Larsen et al. [25] applied a stabilized Reynolds–averaged Navier–Stokes (RANS) model to simulate waves propagating and breaking over a fixed bar. They found that the turbulent kinetic energy peaks reached a lower level near the bar trough compared to those at the bar crest. Wang et al. [26] inferred that the process of stratified water moving over the sandbar may excite internal waves and cause oscillation in the channel. Fang et al. [27] developed a nonlinear Schrödinger (ENLS) equation to investigate the Bragg scattering of nonlinear surface waves by sinusoidal sandbars and found the critical $kh$ ($k$ is the wavenumber, and $h$ is an averaged water depth) increases monotonically with the increase in sandbar amplitude. Gao et al. [28–30] suggested that the Bragg reflection could help reduce the harbor oscillations.

In shallow water, wave propagation over the seabed generates dynamic water pressure at the water–seabed interface. The porous medium model serves as the foundation for many research studies on the wave–induced soil dynamic response. The theoretical model can be split into two versions based on whether the interaction between the pore fluid and soil skeleton is considered: uncoupled model and coupled model. The uncoupled model can describe the flow characteristics of pore fluid in coarse soil, but it is not suitable for seabed with large soil skeleton deformation [31,32]. The motion and dynamic characteristics of soil skeleton and pore fluid are considered in the coupled model. The famous Biot consolidation model, proposed in 1941, provides a comprehensive understanding of the interaction between soil particles and pore water within the seabed soil [33]. Based on the consideration of fluid and soil skeleton acceleration, there are three categories of simplified Biot consolidation models: quasi–static model (QS model), the partially dynamic model ($u$–$p$ model), and the fully dynamic model ($u$–$w$ model) [34]. The acceleration of soil skeleton and pore fluid is not considered in the quasi–static model [35]. Jeng derived the analytical solution of the dynamic response of the seabed of uniform and finite thickness [36] and the theoretical solution of the soil dynamics of the seabed of finite depth and hydraulic anisotropy [37]. The results indicated a 23% difference in the calculated pore water pressure between the hydraulic anisotropy and the hydro–isotropic seabed. However, the influence of inertia term must be considered in the dynamic response of seabed soil under some special wave conditions (such as breaking wave action), so a $u$–$p$ model is proposed based on the quasi–static model. Soil particle acceleration is considered in the $u$–$p$ model, while pore fluid acceleration is ignored. The full dynamic model further considers the effect of pore fluid acceleration on the basis of the $u$–$p$ model. The $u$–$p$ approximation results are in general agreement with those of the fully dynamic model [15]. According to the different constitutive equations, the coupling model can be classified into elastic model and elastoplastic model. The elastic model can be used to analyze the oscillatory response mechanism observed in the experiments, while the elastoplastic model can explain the accumulation of pore pressure. Xu et al. [38] illustrated that the trajectory of soil particles in a poro–elastic seabed is elliptical, while the motion of soil particles in a poro–elastoplastic seabed is in the direction of wave propagation and is accompanied by the accumulation

of vertical displacements. The model considering the elastoplastic constitutive relation of seabed soil is easy to diverge and has poor convergence in numerical calculation. Therefore, when the seabed soil is not too fine and the seabed deformation is not considered, the use of elastic model is an accurate and efficient choice. In addition, Ren et al. [16] found that shear failure is the cause of the initial failure of the dense silty seabed through flume experiments. Tong et al. [39] studied the soil response induced by internal solitary waves with the poroelastic theory and analyzed the impact of soil shear modulus and fluid density profiles on seabed shear failure. Additionally, Zhao et al. [40] demonstrated that the combined action of wave and current may lead to shear failure in submerged breakwater foundation.

Morphodynamic studies of sandbars have received increasing attention in recent years. Rafati et al. [41] used XBeach to simulate sandbar erosion during storms and calculated the cross–shore sediment transport rates. Patrick et al. [42] studied the sandbar migration on the storm timescale with a three–dimensional (3-D) wave–resolving hydro–sedimentary model. They found that sediment resuspension was related to turbulence induced by breaking waves, while sediment transport and seabed evolution were largely determined by the undertow distribution. Shtremel et al. [43] discussed the sandbar migration and corresponding sediment transport on the mildly sloping sandy coast under nonlinear wave transformation. They found that the location of the second harmonic maximum determined the dispersion point of sediment discharge and affected the formation and movement of sandbars. Grossmann et al. [44] indicated that the sandbar moves offshore during storms due to the breaking-induced flows, and onshore during calmer periods.

The aforementioned studies of soil dynamic responses are confined to the flat seabed or sloping seabed, while experiments have showed that there is indeed soil response in the sandbar under wave actions. Mieras et al. [45] measured the wave–induced pore water pressure in a sandbar soil of finite thickness and studied the influence of bed shear stress and horizontal pressure gradient on sheet flow over a sandbar. Anderson et al. [11] indicated that the horizontal and vertical pore pressure within the sandbar may lead to sediment transport and momentary seabed failures. However, the small seabed thickness chosen for their experiments may not be a reasonable simulation for the real ocean environment. Islam et al. [46] indicated that the maximum vertical pressure gradient in the loosely compacted sandbar is 1.3 times greater than that in the medium–dense formations on average. Though previous studies have revealed some features of wave–induced soil response and sandbar morphodynamics, while the motion response and shear failure potential of sandbar topography are poorly understood. This motivates this study, which simulates the sandbar response generated by the wave motion. The effects of wave period, wave height, seabed soil permeability coefficient, soil shear modulus, and saturation level on the sandbar response to the wave loading are simulated.

## 2. Materials and Methods

Numerical models in this research include the fluid model (wave model) and seabed soil model.

### 2.1. Wave Model

In the wave model, water is assumed to be incompressible and the wave motion is simulated by solving the Reynolds–averaged Navier–Stokes (RANS) equations. The mass conservation equation is given by

$$\frac{\partial \langle u_i \rangle}{\partial x_i} = 0 \tag{1}$$

and the momentum equations can be expressed as

$$\frac{\partial (\rho \langle u_i \rangle)}{\partial t} + \frac{\partial (\rho \langle u_i \rangle \langle u_j \rangle)}{\partial x_j} = -\frac{\partial \langle p \rangle}{\partial x_i} + \frac{\partial}{\partial x_i}\left[ \mu \left( \frac{\partial \langle u_i \rangle}{\partial x_j} + \frac{\partial \langle u_j \rangle}{\partial x_i} \right) \right] + \frac{\partial}{\partial x_i}\left( -\rho \langle u'_i u'_j \rangle \right) + \rho g \tag{2}$$

where $x_i$ ($i = x, z$) stands for the Cartesian coordinate, $\langle u_i \rangle$ is the Reynolds–averaged water velocity, $t$ is the time, $\rho$ is the water density, $\langle p \rangle$ is the dynamic pressure, $\mu$ is the dynamic water viscosity, $g$ is the gravity acceleration, and $-\rho \langle u'_i u'_j \rangle$ is the Reynolds stress term. On the basis of the eddy viscosity assumption, the Reynolds stress term can be calculated from

$$-\rho \langle u'_i u'_j \rangle \;=\; \mu_t \left( \frac{\partial \langle u_i \rangle}{\partial x_j} + \frac{\partial \langle u_j \rangle}{\partial x_i} \right) - \frac{2}{3}\rho \delta_{ij} k \tag{3}$$

in which $\mu_t$ represents the turbulent viscosity, $k$ is the turbulence kinetic energy, and $\delta_{ij}$ is the Kronecker delta. On the basis of Equation (3), Equation (2) can be expressed as

$$\frac{\partial (\rho \langle u_i \rangle)}{\partial t} + \frac{\partial (\rho \langle u_i \rangle \langle u_j \rangle)}{\partial x_j} \;=\; -\frac{\partial}{\partial x_i}\left( \langle p \rangle + \frac{2}{3}\rho k \right) + \frac{\partial}{\partial x_i}\left[ \mu_{eff} \left( \frac{\partial \langle u_i \rangle}{\partial x_j} + \frac{\partial \langle u_j \rangle}{\partial x_i} \right) \right] + \rho g \tag{4}$$

where $\mu_{eff} \;=\; \mu + \mu_t$ represents the total effective viscosity and the symbol $\langle\ \rangle$ stands for Reynolds averaging operator. The turbulence kinetic energy $k$ is calculated by solving the standard $k$–$\epsilon$ turbulence model [47]:

$$\frac{\partial \rho k}{\partial t} + \frac{\partial \rho \langle u_j \rangle k}{\partial x_j} \;=\; \frac{\partial}{\partial x_j}\left[ \left( \mu + \frac{\mu_t}{\sigma_k} \right) \frac{\partial k}{\partial x_j} \right] + \rho P_k - \rho \epsilon \tag{5}$$

$$\frac{\partial \rho \epsilon}{\partial t} + \frac{\partial \rho \langle u_j \rangle \epsilon}{\partial x_j} \;=\; \frac{\partial}{\partial x_j}\left[ \left( \mu + \frac{\mu_t}{\sigma_\epsilon} \right) \frac{\partial \epsilon}{\partial x_j} \right] + \frac{\epsilon}{k}(C_{\epsilon 1}\rho P_k - C_{\epsilon 2}\rho \epsilon) \tag{6}$$

$$\mu_t \;=\; \rho C_\mu \frac{k^2}{\epsilon} \tag{7}$$

where $\epsilon$ represents the dissipation rate of the turbulence kinetic energy. $\sigma_k$ and $\sigma_\epsilon$ are Prandtl numbers corresponding to $k$ and $\epsilon$. The empirical coefficients in the equation can generally be taken as $\sigma_k = 1.00$, $\sigma_\epsilon = 1.30$, $C_{\epsilon 1} = 1.44$, $C_{\epsilon 2} = 1.92$, and $C_\mu = 0.09$.

In the numerical model, the waves are generated by an internal wave–making device [48]. In the source region, the mass conservation equation can be expressed as

$$\frac{\partial \langle u_i \rangle}{\partial x_i} \;=\; s(x_i, t) \tag{8}$$

where $s(x_i, t)$ is a source function. The value of $s(x_i, t)$ is determined by the type and characteristics of the wave. According to the wave period and water depth conditions, second–order Stokes waves are generated in this study. The source function of the second–order Stokes wave is given by

$$s(t) \;=\; \frac{CH}{A}\left( \frac{\pi}{2} - \sigma t - p_s \right) + \frac{CH^2 k}{8A} \frac{\cosh kd}{\sinh^3 kd}(2 + \cosh 2kd) \cos\left[ 2\left( \frac{\pi}{2} - \sigma t - p_s \right) \right] \tag{9}$$

in which $C$ is the wave phase velocity, $A$ is the area of the source region, $\sigma$ is the wave frequency, and $k$ is the wave number; $p_s$ is the phase shift constant, which is designed to ensure that both $\eta$ and $s$ start from zero at $t = 0$ and can be expressed as

$$p_s \;=\; \arcsin\left( \frac{-a_s + \sqrt{a_s^2 + 8b_s^2}}{4b_s} \right) \tag{10}$$

where

$$a_s \;=\; \frac{H}{2}, \; b_s \;=\; H^2 k \cosh \frac{kd(2 + \cosh 2kd)}{16\sinh^3 kd} \tag{11}$$

The wave model employs the volume of fluid (VOF) method [49] to monitor the water–air interface. The RANS governing equations can be solved using the finite difference

method. The time derivative is discretized using the forward time difference method. The spatial derivations are computed using a combination of the upwind scheme and the central difference scheme. More details can be found in Zhang et al. [50].

*2.2. Seabed Model*

The partially dynamic model (*u–p* model) is employed to study the dynamic responses of the seabed during the wave shoaling process, as it can consider the acceleration effect of the soil skeleton on the soil dynamics. The continuity equation is given by [51]

$$\frac{k_s}{\gamma}\nabla^2 p - \frac{n}{K'}\frac{\partial p}{\partial t} + \frac{k_s}{g}\frac{\partial^2 \varepsilon}{\partial t^2} = \frac{\partial \varepsilon}{\partial t} \tag{12}$$

in which $k_s$ is the coefficient of permeability of the soil, $\gamma$ is the unit weight of the pore fluid, $p$ is the excess pore water pressure, $n$ is the porosity, $K'$ is the apparent bulk modulus of elasticity of the pore fluid, and $\varepsilon$ is the volume strain of the porous medium. When the pore water contains a small amount of air, the apparent bulk modulus of elasticity of the water decreases sharply and $K'$ can be expressed in relation to saturation as

$$\frac{1}{K'} = \frac{1}{K} + \frac{1 - S_r}{P_0} \tag{13}$$

where $K$ is the bulk of modulus of pore water and is equal to $2 \times 10^9$ N/m$^2$. $S_r$ is the degree of saturation and $P_0$ is the absolute pore water pressure. The volume strain for the two–dimensional problem is

$$\varepsilon = \frac{\partial u}{\partial x} + \frac{\partial w}{\partial z} \tag{14}$$

where $u$ and $w$ represent the soil displacements in the *x*-direction and *z*-direction, respectively.

According to the Hooke's law, the momentum equations are given by

$$G\nabla^2 u + \frac{G}{1 - 2\nu}\frac{\partial \varepsilon}{\partial x} = -\frac{\partial p}{\partial x} + \rho\frac{\partial^2 u}{\partial t^2} \tag{15}$$

$$G\nabla^2 w + \frac{G}{1 - 2\nu}\frac{\partial \varepsilon}{\partial z} + \rho g = -\frac{\partial p}{\partial z} + \rho\frac{\partial^2 w}{\partial t^2} \tag{16}$$

where $\nu$ is Poisson's ratio for the soil, $G$ is the shear modulus of the soil, and $\rho = \rho_f n + \rho_s(1 - n)$ is the bulk density of the soil.

*2.3. Boundary Conditions*

The coordinate system and boundary conditions employed in this study are shown in Figure 1. The pore water pressure is equivalent to the dynamic wave pressure at the seabed surface, where the vertical effective stress and shear stress vanish:

$$p_s = p_b, \ \tau_{zz} = 0, \ \tau_{xz} = 0 \text{ at } Z = 0 \tag{17}$$

in which $p_b$ is the dynamic wave pressure at the water–seabed interface obtained from wave model. No–slip and no–flux boundary conditions at the bottom of the seabed are

$$\frac{\partial p}{\partial z} = u_s = w_s = 0 \text{ at } Z = -d \tag{18}$$

This model allows for calculations of the dynamic response inside the seabed under different soil properties, like permeability, shear modulus, and saturation.
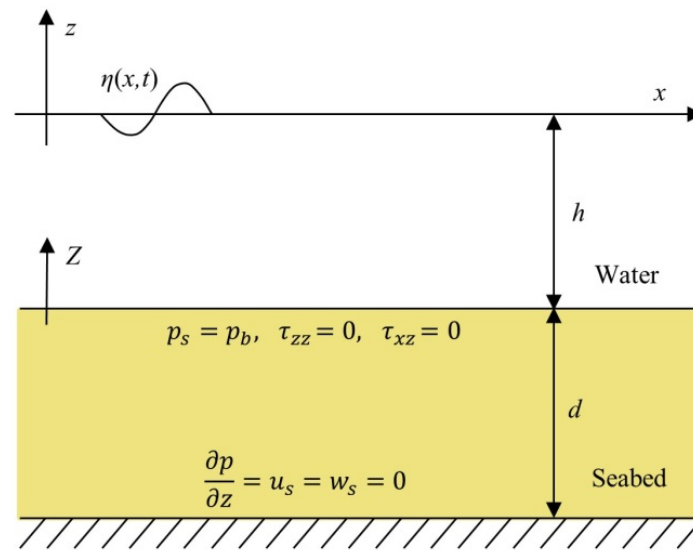
**Figure 1.** Schematic diagram of a wave propagating on a seabed.

*2.4. Model Coupling and Validation*

The two models will be integrated through the continuity of velocity and pressure on the seabed surface. Separate meshes are used for the wave model and seabed model. The wave model and seabed model are integrated using a one–way coupling. The wave model will be run first to calculate the velocity and pressure fields. The results of the wave model calculations are interpolated using the radial point interpolation meshless method (radial PIM) [52]. Then, the converted dynamic wave pressure on the seabed surface is used as the boundary condition of the seabed model to calculate the pore water pressure, soil particle displacement, and effective stress around the sandbar.

The numerical model is validated using two experiments conducted by Mieras et al. [45] and Anderson et al. [11]. The wave flume is 104 m long, 3.7 m wide, and 4.6 m deep. In the experiment, waves were generated by a programmable piston–type wave maker. Based on the DUCK94 field experiment, a fixed concrete beach profile with a sand pit at the highest point of the bar profile was constructed. The sand pit was 3.66 m long, 3.66 m wide, and 0.18 m deep, filled with sand with an average grain size of 0.17 mm. Instruments were accommodated by adding a secondary square pit at the center of the pit, measuring 1.22 m × 1.22 m and with a depth of 0.43 m, as shown in Figure 2a. Seven pore–pressure transducers with 2 cm spacing (center–to–center) were used to measure pore pressures. Five transducers (P1–P5) formed the horizontal row located 5–10 mm below the initial bed level, and two transducers (P6, P7) extended vertically beneath the center transducer, as shown in Figure 2b,c. In the experiment, the wave maker had a still water depth of 2.45 m, while over the sandbar it was 1 m. The wave height was 0.6 m and the wave period was 7 s in the test. The experiments did not involve direct measurements of saturation degree and soil shear modulus. Due to the consolidation conditions and mean grain diameter of sand being similar to those in Zhai's experiments, we use Zhai's measurement results to determine the soil saturation and shear modulus [53]. The soil saturation and shear modulus are estimated to be 0.982 and $8 \times 10^6$ Pa, respectively, which results in a bulk elastic modulus $K$ of $5.4 \times 10^5$ Pa for the pore fluid. More detailed seabed soil properties of the laboratory experiments are summarized in Table 1.
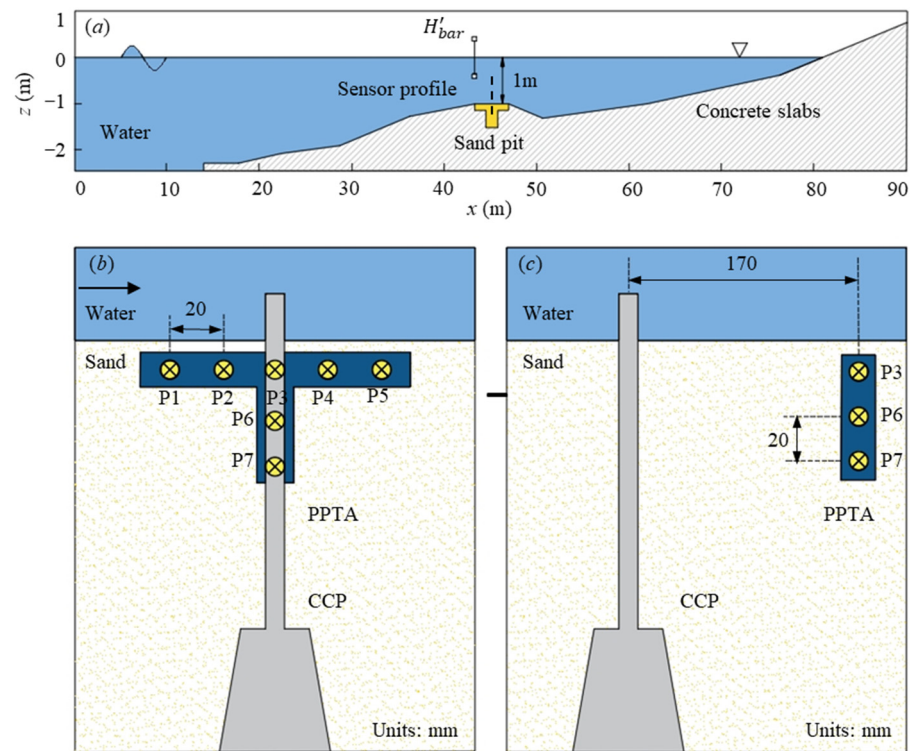
**Figure 2.** Experimental setup and instrument arrangement in Mieras et al. [45]: (**a**) beach profile; (**b**) the spanwise view of the Pore–Pressure Transducer Array (PPTA) and Conductivity Concentration Profiler (CCP) in the sandy bed; (**c**) the onshore view of sensor proximities.

**Table 1.** Test conditions of the experiments.

| Mediums | Parameters | Symbol | Value |
|---------|-----------|--------|-------|
| Seabed | Soil depth (m) | $d$ | 0.18 |
| | Soil porosity | $n$ | 0.40 |
| | Poisson's ratio | $\nu$ | 0.35 |
| | Saturation degree | $S_r$ | 0.982 |
| | Permeability coefficient (m$^2$) | $k_s$ | $2.85 \times 10^{-10}$ |
| | Bulk elastic modulus of pore fluid (Pa) | $K$ | $5.4 \times 10^5$ |
| | Shear modulus of the seabed (Pa) | $G$ | $8.0 \times 10^6$ |
| Wave | Water depth (m) | $h$ | 1 |
| | Wave period (s) | $T$ | 7 |
| | Wave height (m) | $H$ | 0.6 |

Figure 3 displays the contrast of the numerically simulated and experimentally measured free–surface elevation (Figure 3a), wave–induced pore pressure (Figure 3b), and the horizontal pressure gradient at P3 (Figure 3c). It shows that the numerical simulation results and experimental results are highly in agreement. Some difference is observed near the wave crest in Figure 3b,c. This could be because the wave gauge was 1.83 m away from the pore–pressure transducer in the experiments. Using the same wave flume as Mieras et al. [45], Anderson et al. [11] measured the phase–average vertical pressure gradient over 10 wave cycles at P3. Figure 4 is the simulated free-surface elevation, horizontal, and vertical pressure gradients at P3 compared with the measured results of Anderson et al. [11]. Overall, the numerical and experimental results show good consistency in phase and amplitude. The distinction between the experimental results and numerical simulation can be attributed to the fact that Anderson et al. [11] selected the average values of ten periodic waves for data analysis.
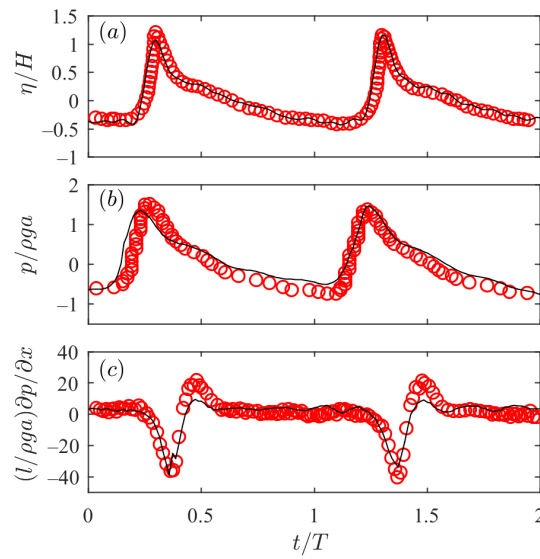
**Figure 3.** Comparison of the numerical simulation and experimental measurements in Mieras et al. [45]. (**a**) The free surface; (**b**) the wave–induced water pressure; (**c**) the horizontal water pressure gradient. Symbols: red cycles: experiments; black lines: numerical simulation.
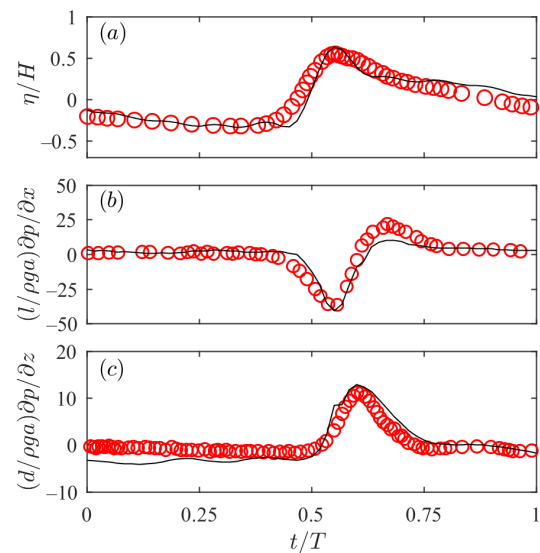


**Figure 4.** Comparison of the numerical simulation and experimental results in Anderson et al. [11]. (**a**) The free surface; (**b**) the vertical water pressure gradient; (**c**) the horizontal water pressure gradient. Symbols: red cycles: experiment; black lines: numerical simulation.

## 3. Results and Discussion

The comparisons of the numerical and experimental results indicate that this model is suitable for studying wave–induced soil response around the sandbar with satisfactory accuracy. In the field, the sandbar is formed by sand and the thickness of the seabed is usually larger than the height of the sandbar. However, in the experiments of Mieras et al. [45], partly owing to the limitations of the flume, the sandy seabed thickness was set to 0.18 m, which is much smaller than the height of the sandbar. Previous studies had demonstrated that the seabed thickness had significant effects on wave–induced seabed soil responses [54], suggesting that the pore pressure and its gradients might be underestimated when the seabed thickness was smaller than that of the sandbar. Jeng and Cha [15] also indicated that the distribution of shear stress is significantly affected by the seabed thickness. In this numerical study, we set the seabed thickness to 6.5 m (larger than the sandbar thickness) to research the wave–generated pore pressure and the

effective stresses. Figure 5 is the two–dimensional computational domain which is 260 m long ($-140$ m $< x <$ 120 m) and 10.5 m high ($-7.5$ m $< z <$ 3 m). The internal wave–making device is located at $x = -90$ m. The grid is uniform, with a horizontal grid spacing of 0.1 m and a vertical grid spacing of 0.02 m. The total duration of the simulation is from 0 s to 150 s, with a time interval of 0.1 s. To prevent the influence of wave reflection, the left side of the flume is set as an open boundary. In the seabed model, the triangular element meshes are used to discrete the calculation domain. After the convergence test, the maximum length of the edge of the triangle is 0.154 m.
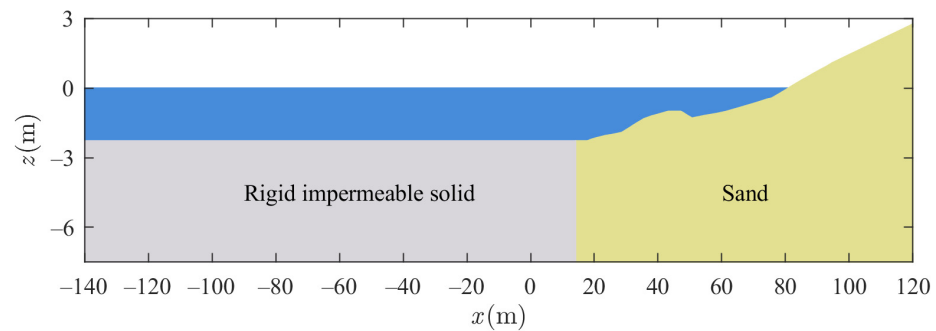


**Figure 5.** Schematic diagram of the computational domain.

The wave conditions used in numerical cases are summarized in Table 2. In the table, the incident wave type is determined based on the nonlinearity parameter (wave height divided by wavelength) and frequency dispersion parameter (water depth divided by wavelength) [55]. As shown in Figure 6, the wave conditions covered in this paper all lie in the range of second–order stokes waves. In all cases, the soil properties are the same as those in the experiments (see Table 1).

**Table 2.** Summary of wave cases with wave conditions and wave types.

| Case | Water Depth $h$ (m) | Wave Period $T$ (s) | Wave Height $H$ (m) | Wavelength $L$ (m) | $h/L$ | $H/L$ | Wave Type |
|---|---|---|---|---|---|---|---|
| 1 | 2.28 | 5 | 0.4 | 34.3 | 0.22 | 0.0117 | second–order stokes wave |
| 2 | 2.28 | 5 | 0.5 | 34.3 | 0.22 | 0.0146 | second–order stokes wave |
| 3 | 2.28 | 5 | 0.6 | 34.3 | 0.22 | 0.0175 | second–order stokes wave |
| 4 | 2.28 | 7 | 0.4 | 53.9 | 0.14 | 0.0074 | second–order stokes wave |
| 5 | 2.28 | 7 | 0.5 | 53.9 | 0.14 | 0.0093 | second–order stokes wave |
| 6 | 2.28 | 7 | 0.6 | 53.9 | 0.14 | 0.0111 | second–order stokes wave |
| 7 | 2.28 | 9 | 0.4 | 72.4 | 0.1 | 0.0055 | second–order stokes wave |
| 8 | 2.28 | 9 | 0.5 | 72.4 | 0.1 | 0.0069 | second–order stokes wave |
| 9 | 2.28 | 9 | 0.6 | 72.4 | 0.1 | 0.0083 | second–order stokes wave |

Figure 7a,b displays the time histories of wave-induced soil displacements at various depths in the sandbar. It is indicated that soil displacements change periodically under wave load, and the time history curves at different depths have no phase difference. There is little difference between the horizontal soil displacement at $z = -2$ cm and $z = -4$ cm, while it decreases significantly in the range from $z = -4$ cm to $z = -6$ cm. The soil vertical displacement declines evenly along soil depth. Figure 7c shows that pore pressure decreases significantly from $z = -2$ cm to $z = -4$ cm. The attenuation of pore water pressure decreases with increasing depth. The difference in pore water pressure between $z = -4$ cm and $z = -6$ cm is negligible. As the seabed depth grows, the horizontal effective stress declines, and the trough of the time history curve flattens gradually. As shown in Figure 7e, there are obvious phase differences of vertical effective stress at different depths. In addition, the effective vertical stress at $z = -4$ cm is less than that at $z = -2$ cm and $z = -6$ cm.

Compared with Figure 7d–f, it is evident that the shear stress in the sandbar is less than the effective stresses.



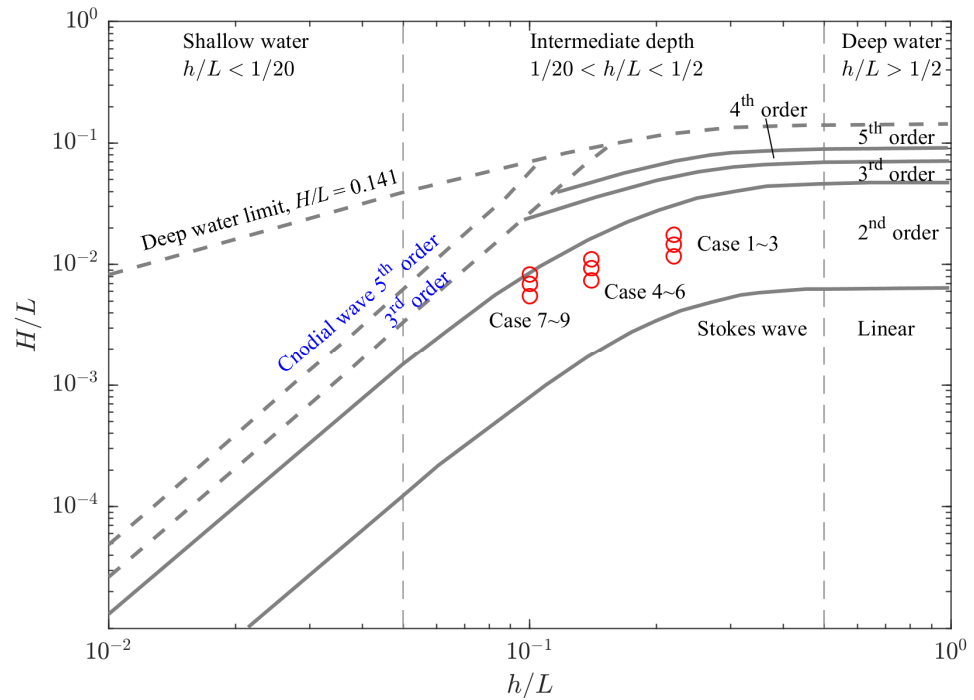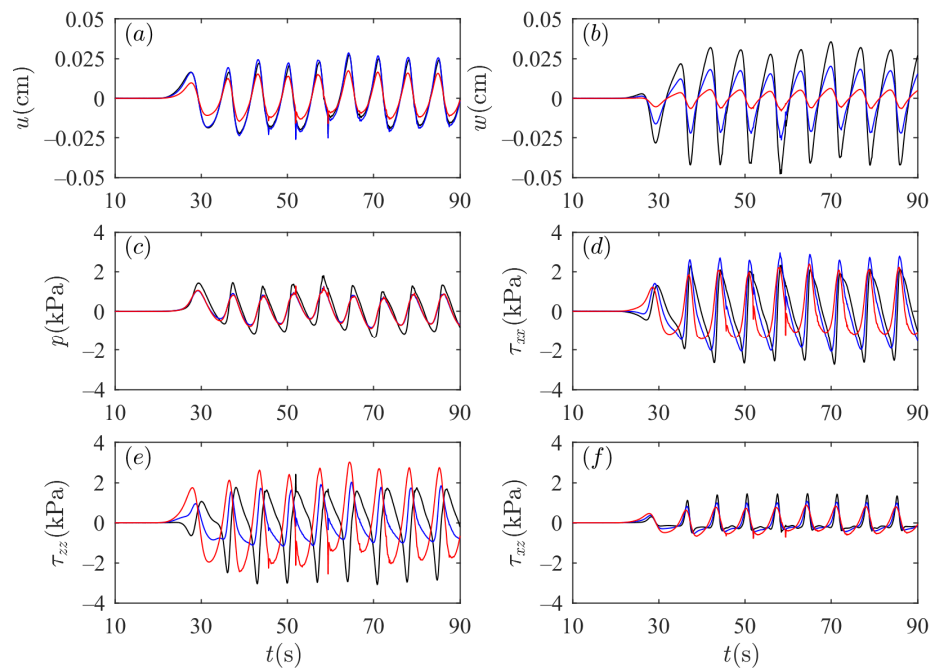**Figure 6.** The application range of various wave theories in Zhao et al. [55].



**Figure 7.** Time histories of the (**a**) horizontal soil displacement, (**b**) vertical soil displacement, (**c**) pore pressure, (**d**) horizontal effective stress, (**e**) vertical effective stress, (**f**) shear stress at various depths in Case 6. Symbols: black lines: $z = -2$ m; blue lines: $z = -4$ m; red lines: $z = -6$ m.

Figures 8 and 9 show the simulated contours of the pore pressure, soil particle displacement, and effective stresses around a sandbar. At the sandbar surface, the pore pressure hits its peak at the moment of wave crest, when the wave dynamic pressure is the largest. The horizontal displacement of soil particles reaches the maximum value in front of the

wave crest and the minimum value near the still water level. When the waves propagate near the sandbar, the crest becomes sharp and steep, while the trough becomes flat. The water particle path over one wave cycle is not a closed orbit. This may explain why the maximum horizontal displacement occurs in front of the wave crest. Furthermore, the vertical particle displacement is positive at the wave trough and is negative at the wave crest. This is because the pore pressure decreases by increasing soil depth, resulting in a downward vertical pore pressure gradient. Under the wave crest, the soil skeleton is compressed by the downward vertical pore pressure gradient. However, under the wave trough the pressure gradient reverses its direction, creating a positive vertical normal stress in the seabed. The vertical effective stress, $\tau_{zz}$, and the horizontal effective stress, $\tau_{xx}$, are significantly larger than shear stress, $\tau_{xz}$, The shear stresses reach the maximum value in front of the wave crest and the minimum value near the still water level. Compared to the seabed surface, the effective stress distribution at the seabed bottom shows a trend of shifting towards the shore, which may be attributed to the slope of the seabed topography.
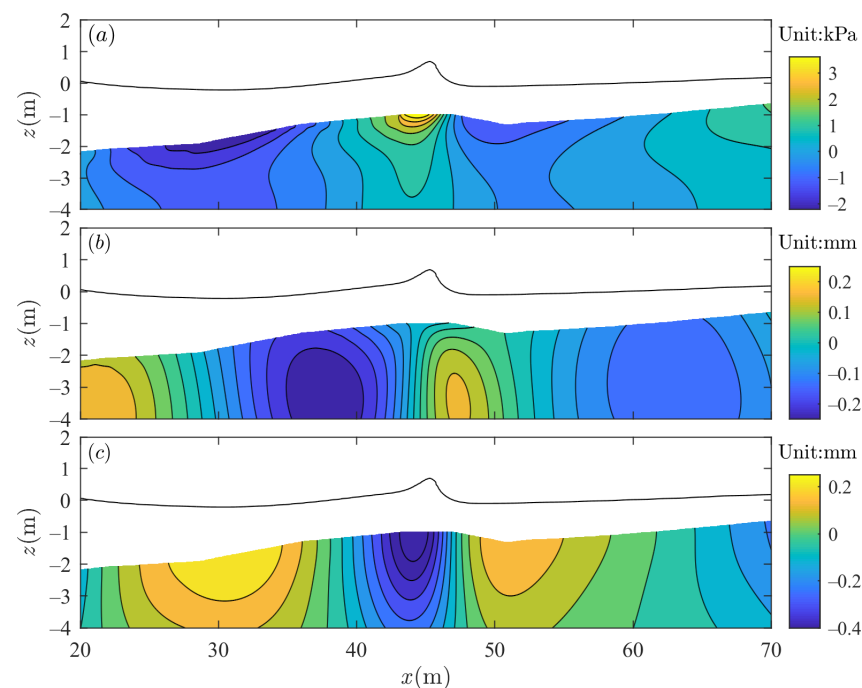


**Figure 8.** Contour plots of pore pressure and soil particle displacement around a sandbar: (**a**) pore pressure *p*; (**b**) horizontal particle displacement *u*; (**c**) vertical particle displacement *w*.

### 3.1. Effects of Wave Characteristics on Soil Dynamics around the Sandbar

As a demonstration, the seabed soil response around the sandbar (e.g., *x* = 45.1 m, see Figure 5) is selected to examine the impact of wave characteristics (e.g., wave period, wavelength, and wave height) on the distribution of the maximum value of pore pressure, soil particle displacement, and effective stresses. When the water depth is constant, changing the wave period also means changing the wavelength. The wave periods simulated are 5 s, 7 s, and 9 s and the corresponding wavelengths are 23.09 m, 33.48 m, and 43.65 m, respectively.

The distribution of the maximum pore pressure, soil particle displacement, and effective stresses along the central profile of a sandbar with different wave periods are shown in Figure 10. A growth in the maximum pore pressure with increasing wave period can be observed, which is consistent with the simulations in a flat seabed [15]. This is attributed to the fact that the wave with a longer wave period/length has longer loading acting on the seabed than that with a shorter period/length for otherwise identical conditions. The pore pressure decreases from the sandbar surface to the bottom. Waves of different periods all exhibit a sharp decline in the pore pressure within the range of *z* = −1 m, followed by

a relatively gradual drop of the pore pressure within the range of $z = -1$ m to $-6.5$ m, which is consistent with the vertical distribution of the maximum pore pressure amplitude along the soil depth in a horizontal flat seabed mentioned by Jeng and Lin [56]. This can be ascribed to the fact that wave energy damps quickly near the seabed surface and the wave energy damping rate declines as soil depth increases. In comparison to Case 2, the relative growth of the pore pressure at the seabed bottom is, respectively, 53.58% and 138.35%, with the wave period increasing by 40% and 80% in Case 5 and Case 8.
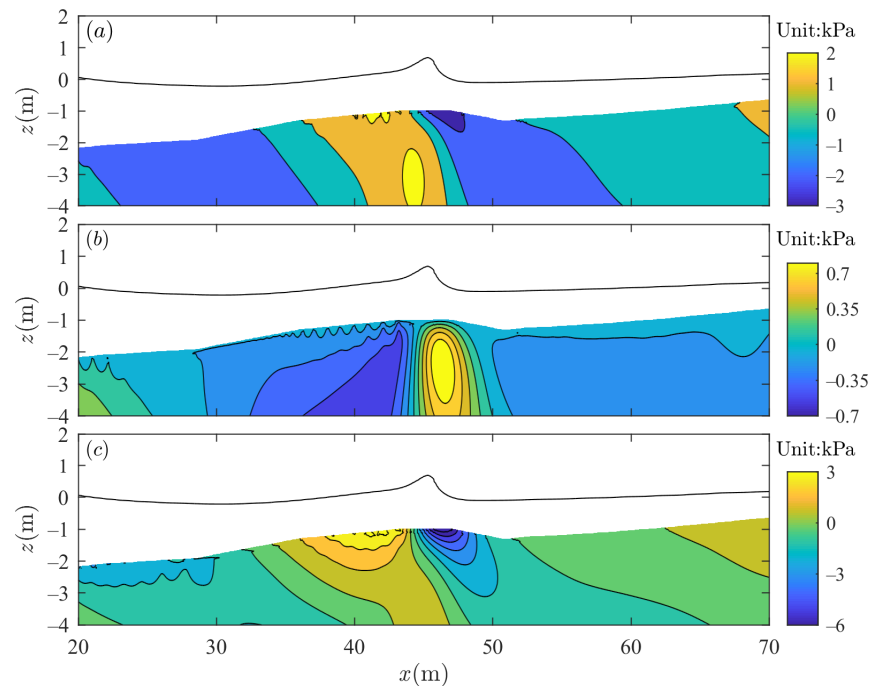


**Figure 9.** Contour plots of effective stresses around a sandbar: (**a**) horizontal effective stress $\tau_{xx}$; (**b**) shear stress $\tau_{xz}$; (**c**) vertical effective stress $\tau_{zz}$.

The maximum horizontal displacement of soil grows as the wave period increases, while the vertical displacement of soil is not affected by the wave period. For a small wave period, the maximum soil particle horizontal displacement grows linearly at first, then increases gradually, and decreases to zero within the depth range of $z = -6.5$ m to $-2$ m. As the wave period increases, the linearly increasing portion decreases. When $T = 9$ s, the maximum soil particle horizontal displacement grows first and then declines with the soil depth. Similar trends can also be observed in Jeng and Rahman's study [14]. In comparison to Case 2, the relative enhancements of the maximum horizontal displacement at the seabed surface are, respectively, 29.19% and 36.05%, with the wave period increasing by 40% and 80% in Case 5 and Case 8. Both the horizontal and vertical displacement decrease to zero near the seabed bottom, which is owing to the boundary conditions of the seabed model.

The maximum values of effective stresses and shear stress increase with an increasing wave period in the sandbar. Whereas, on the flat seabed, the shear stress decreases with an increasing wave period [15]. The maximum horizontal effective stress shows an S–shaped distribution and then slightly increases from $z = -6.5$ m to $-5.8$ m along soil depth. This may be influenced by the relative compressibility of soil and pore fluid [57]. The S–shaped vertical distribution of the horizontal effective stress is identical to that in a horizontal flat seabed with the dimensionless seabed thickness $d/L = 0.2$–$0.3$ simulated by Jeng and Rahman [14]. The dimensionless seabed thickness $d/L$ for the three cases in Figure 10 ranges from 0.09 to 0.19. The vertical effective stress decreases to the minimum from the water–seabed interface to around $z = -1.45$ m and increases with increasing soil depth. According to Jeng and Rahman [14], the vertical effective stress in flat seabed first grows and then declines along seabed depth, which differs from the results in Figure 10e. Because

of the sandbar's slope and nonlinear processes, waves will always get steeper as they move nearer it. The wave shoaling may lead to differences in the distribution of vertical effective stress in the sandbar and flat seabed. The maximum value of shear stress increases first and then decreases within the depth range of $z = -4.7$ m to $-1.35$ m. It increases from $z = -4.7$ m to the seabed bottom. The zero-shear stress on the seabed surface is confined by the boundary conditions set in the seabed model. Comparing Case 2 and Case 8, the horizontal effective stress, vertical effective stress, and shear stress at the seabed bottom in Case 8 increase by 144.45%, 144.45%, and 144.44%, respectively, as the wave period increases by 80% from Case 2 to Case 8. The results indicate that the variation amplitudes of effective stresses and shear stress in the soil are the same when the wave period changes.
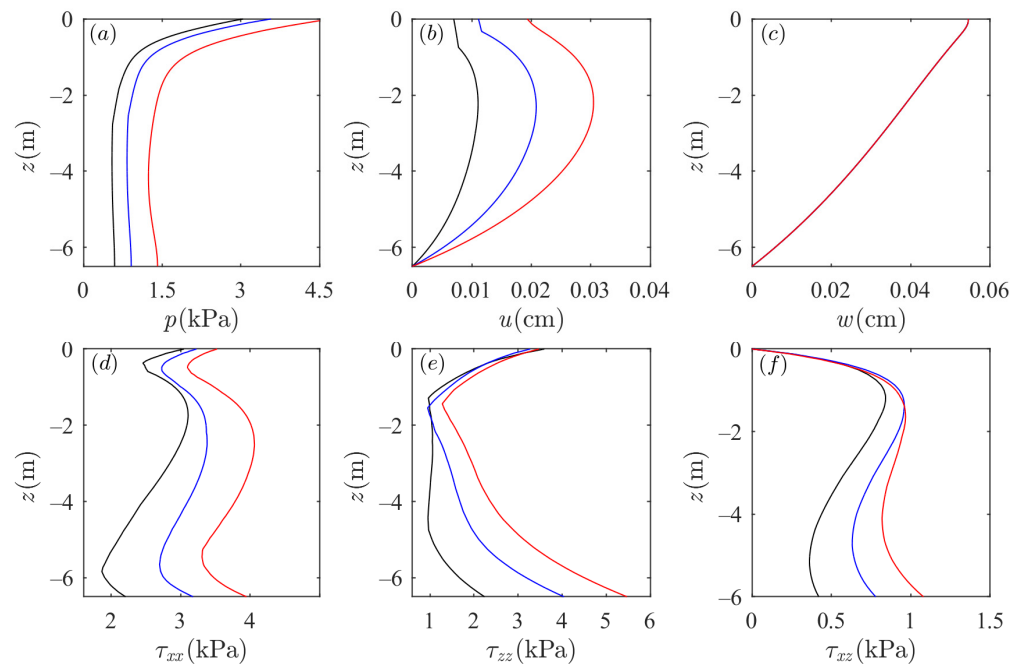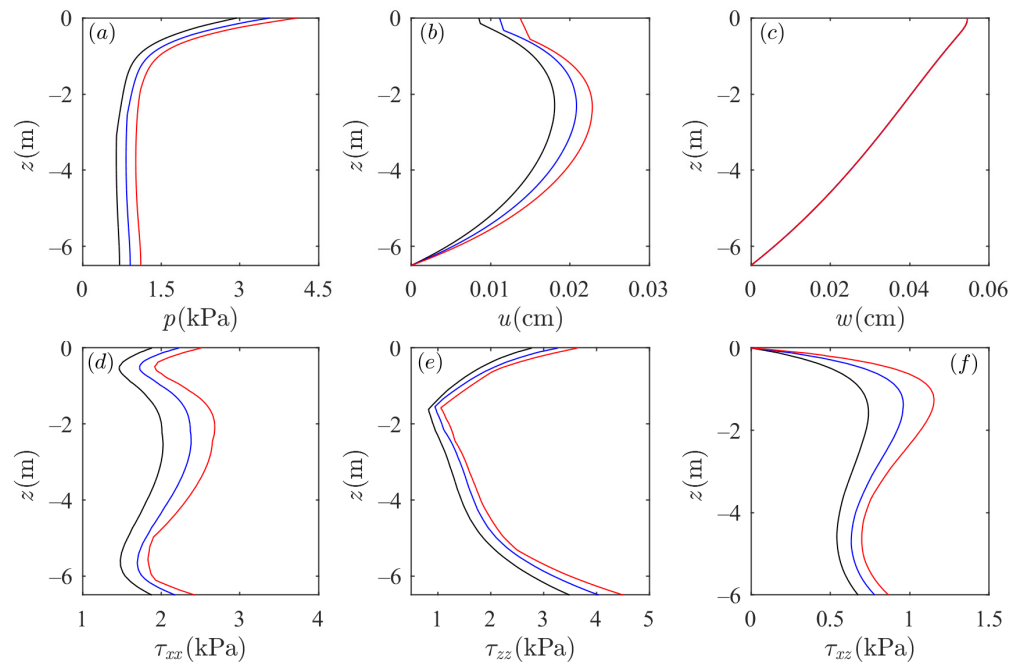


**Figure 10.** Effects of wave period on (**a**) pore pressure, (**b**) horizontal particle displacement, (**c**) vertical particle displacement, (**d**) horizontal effective stress, (**e**) vertical effective stress, and (**f**) shear stress profile. Symbols: black line: Case 2; blue line: Case 5; red line: Case 8.

Wave pressure consists of static water pressure and dynamic water pressure. When the water depth is constant, the static water pressure remains the same. The larger the wave height, the greater the amplitude of wave surface fluctuations, resulting in increased dynamic water pressure and correspondingly increased wave energy. Cases 4–6 are taken as examples to study the impact of wave height on the wave-induced soil dynamic response around a sandbar.

Figure 11 reveals that the maximum pore pressure and the maximum horizontal particle displacement increase with increasing wave height, while the distribution of the maximum vertical particle displacement does not change with the change in wave height. Compared with Case 4, the relative increasements of dynamic pore pressure at the sandbar surface are 28.7% and 57.29% for the wave height in front of the wave maker increased by 25%, and 50% in Case 5 and Case 6. The results denote that the impact of wave height on pore pressure is nonlinear. This may be due to the nonlinear terms in the governing equation of the wave model. Meanwhile, the maximum effective stresses and shear stress increase as wave height increases. Comparing Case 4 and Case 6, when the wave height increases by 50%, the horizontal effective stress, vertical effective stress, and shear stress at the seabed bottom increase by 29.01%, 29.02% and 29.01%, respectively. It can be illustrated that the impacts of wave height on the maximum values of effective stresses and shear stress are basically the same. The effects of wave height on vertical distributions of pore

pressure, vertical effective stress, and shear stress in the sandbar are consistent with that in a flat seabed [15].



**Figure 11.** Effects of wave height on (**a**) pore pressure, (**b**) horizontal particle displacement, (**c**) vertical particle displacement, (**d**) horizontal effective stress, (**e**) vertical effective stress, and (**f**) shear stress profile. Symbols: black line: Case 4; blue line: Case 5; red line: Case 6.

### 3.2. Effects of Seabed Conditions on Soil Dynamics around the Sandbar

Soil properties, such as the permeability coefficient $k_s$, seabed shear modulus $G$, and bulk elastic modulus of pore fluid $K$ (related to the saturation degree $S_r$), have a large impact on wave-induced soil response. To this end, several simulations are preformed to assess the influence of soil properties on soil dynamics around a sandbar. The soil characteristics simulated are recorded in Table 3 and the wave conditions are the same as those in Case 6.

**Table 3.** Summary of soil cases with soil properties.

| Case | $v$ | Porosity $n$ | Shear Modulus $G$ (Pa) | Bulk Modulus of Elasticity of the Pore Fluid $K$ (Pa) | Permeability Coefficient $k_s$ (m/s) |
|---|---|---|---|---|---|
| 10 | 0.35 | 0.4 | $8 \times 10^6$ | $2 \times 10^7$ | $10^{-5}$ |
| 11 | 0.35 | 0.4 | $8 \times 10^6$ | $2 \times 10^7$ | $10^{-4}$ |
| 12 | 0.35 | 0.4 | $8 \times 10^6$ | $2 \times 10^7$ | $10^{-3}$ |
| 13 | 0.35 | 0.4 | $8 \times 10^5$ | $2 \times 10^7$ | $10^{-4}$ |
| 14 | 0.35 | 0.4 | $8 \times 10^7$ | $2 \times 10^7$ | $10^{-4}$ |
| 15 | 0.35 | 0.4 | $8 \times 10^6$ | $5 \times 10^6$ | $10^{-4}$ |
| 16 | 0.35 | 0.4 | $8 \times 10^6$ | $2 \times 10^9$ | $10^{-4}$ |

Figure 12 reveals that the maximum pore pressure grows with increasing soil permeability from the seabed surface to $z = -5.28$ m, and declines to the seabed bottom. The pore pressure at the seabed surface remains constant and is not affected by the permeability coefficient. This is because the pore pressure at the seabed surface is only influenced by the wave pressure. Influenced by the soil permeability, the maximum pore pressure occurs at the seabed surface, and it gradually decreases with increasing seabed depth. This is because, under the wave load, a larger permeability coefficient leads to faster fluid movement within

the pores between soil particles, resulting in a rise in oscillating pore water pressure. With the increasing seabed permeability, the maximum of the horizontal particle displacement increases and becomes unaffected by permeability until the seabed bottom. The maximum vertical particle displacement decreases from the seabed surface to $z = -1$ m, and then becomes unaffected by the change in permeability. The distributions of horizontal effective stress within the soil increase first and then decrease as the soil permeability increases along the soil depth. In the range from the seabed surface to $z = -1.7$ m, the effect of permeability on the vertical effective stress is not significant. In the range from $z = -1.7$ m to the seabed bottom, the vertical effective stress increases and then decreases as permeability increases. Figure 12f indicates that the maximum shear stress increases by increasing soil permeability.
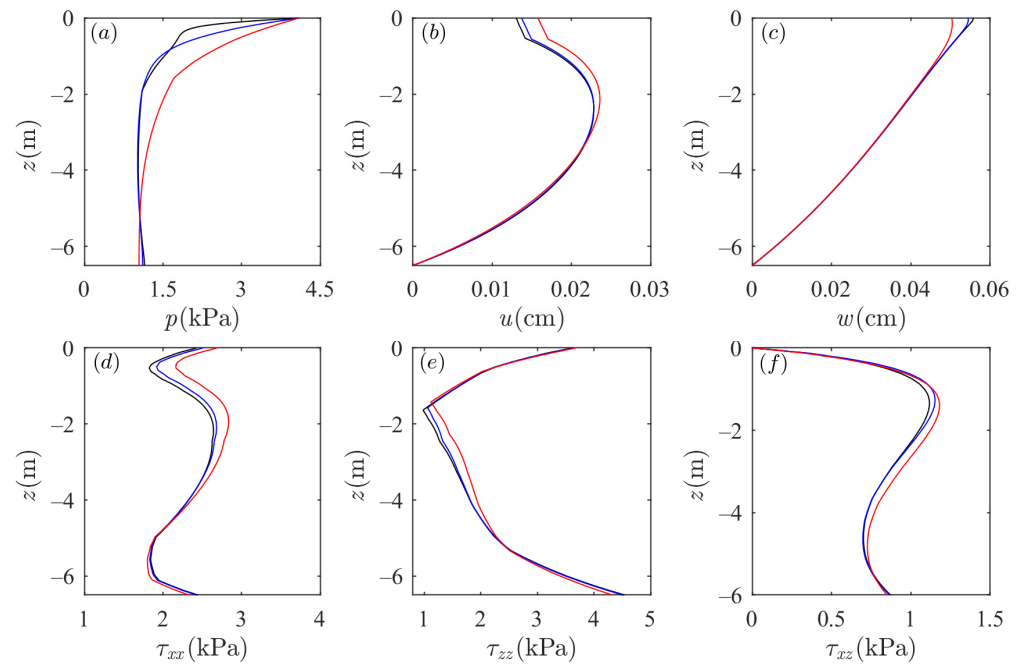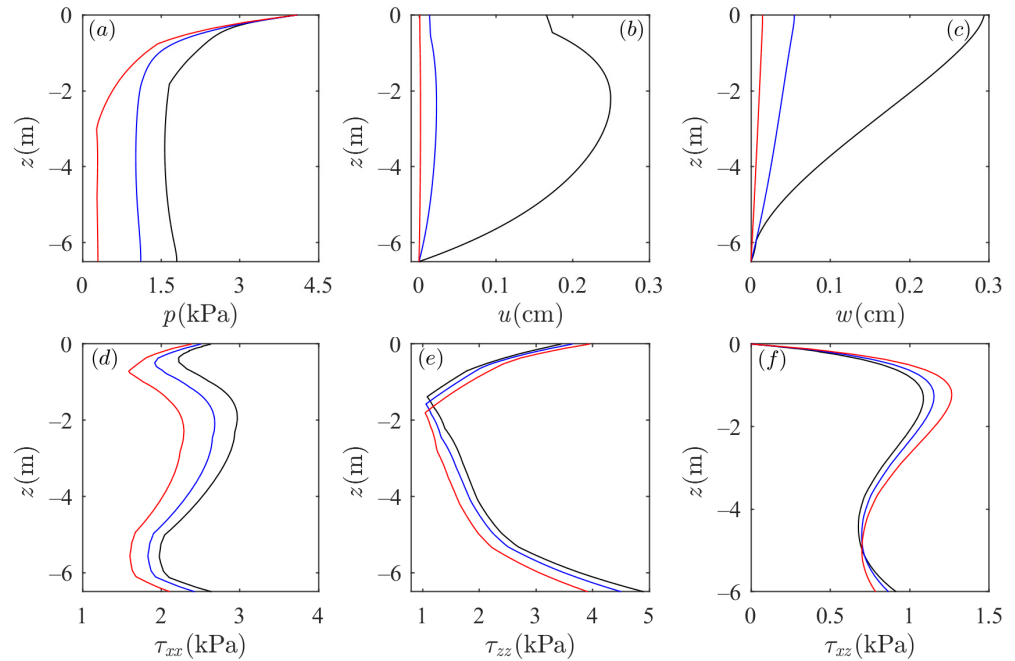


**Figure 12.** Effects of permeability on (**a**) pore pressure, (**b**) horizontal particle displacement, (**c**) vertical particle displacement, (**d**) horizontal effective stress, (**e**) vertical effective stress, and (**f**) shear stress profile. Symbols: black line: $k_s = 10^{-5}$ m/s; blue line: $k_s = 10^{-4}$ m/s; red line: $k_s = 10^{-3}$ m/s.

Figure 13 shows that an increase in shear modulus will reduce the maximum pore water pressure, as well as the maximum particle displacements in the seabed. This is because, in unsaturated soil, as the shear modulus of the seabed increases, the stiffness increases, and the compression of pore volume in soil particles becomes smaller. As a result, the pore water pressure and the soil particle displacement decrease. With the increasing shear modulus of the seabed, the maximum horizontal effective stress within the soil decreases. The maximum vertical effective stress increases first from the seabed surface to $z = -1.55$ m and then declines until the seabed bottom. The distribution of shear stress shows a similar trend as that of the vertical effective stress, with its inflection point at $z = -5$ m. When considering changes of the same order of magnitude, the kinematic and dynamic response of soil is more susceptible to the shear modulus than the permeability coefficient.

According to Equation (13), soil saturation can be adjusted by altering the effective bulk elastic modulus of the fluid. Results in Figure 14 indicate that the dynamic and motion response of the soil around the sandbar is sensitive to changes in saturation. With the increase in seabed soil saturation, the maximum pore water pressure increases, which is consistent with the results in the flat seabed [15,58]. This can be ascribed to the fact that, with the increase in seabed soil saturation, the air content within the soil pores decreases, leading to a more efficient conduction of wave loads. The horizontal displacement of soil particles and horizontal effective stress increase with the increasing soil saturation, while the vertical displacement of soil particles decreases. The vertical effective stress within the

soil decreases from seabed surface to about $z = -1.6$ m, reaching a minimum value and then increases with the increasing soil saturation. Nevertheless, the vertical distribution of vertical effective stress in the flat seabed declines when soil saturation grows [15,58]. The distribution of shear stress exhibits a tendency to increase and then decrease as soil saturation increases.



**Figure 13.** Effects of shear modulus on (**a**) pore pressure, (**b**) horizontal particle displacement, (**c**) vertical particle displacement, (**d**) horizontal effective stress, (**e**) vertical effective stress, and (**f**) shear stress profile. Symbols: black line: $G = 8 \times 10^5$ Pa; blue line: $G = 8 \times 10^6$ Pa; red line: $G = 8 \times 10^7$ Pa.
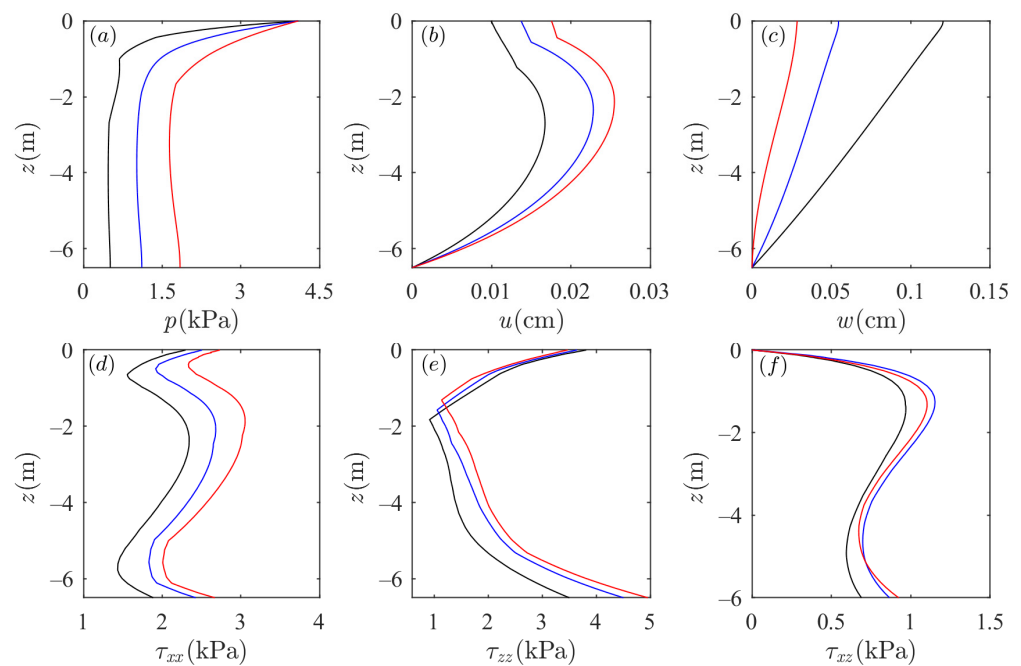


**Figure 14.** Effects of saturation degree on (**a**) pore pressure, (**b**) horizontal particle displacement, (**c**) vertical particle displacement, (**d**) horizontal effective stress, (**e**) vertical effective stress, and (**f**) shear stress profile. Symbols: black line: $S_r = 0.98$; blue line: $S_r = 0.995$; red line: $S_r = 1$.

### 3.3. Wave-Induced Shear Failure around the Sandbar

In engineering practice, it is possible for the seabed to face shear failure under the wave load. The seabed in an offshore environment undergoes an initial consolidation process due to gravity and hydrostatic pressure. From the perspective of soil mechanics, the initial consolidation state of the seabed should be first considered before modeling the wave–seabed interaction.

When gravity and hydrostatic water pressure are applied, the seabed's initial consolidation state is depicted in Figure 15. The seabed parameters are as follows: soil porosity $n = 0.4$, shear modulus $G = 8 \times 10^6$ Pa, and the soil permeability coefficient $k_s = 10^{-4}$ m/s. From Figure 15, the pore pressure and effective stresses are distributed in layers around the sandbar, which is the result of the body forces of seabed foundation. The distribution of shear stress $\tau_{xz}$ shows that there is a concentrated shear stress zone within the trailing edge of the sandbar in the range of $x = 47.5$ m~50.5 m, which is a weak area where shear failure of the sandbar may occur.
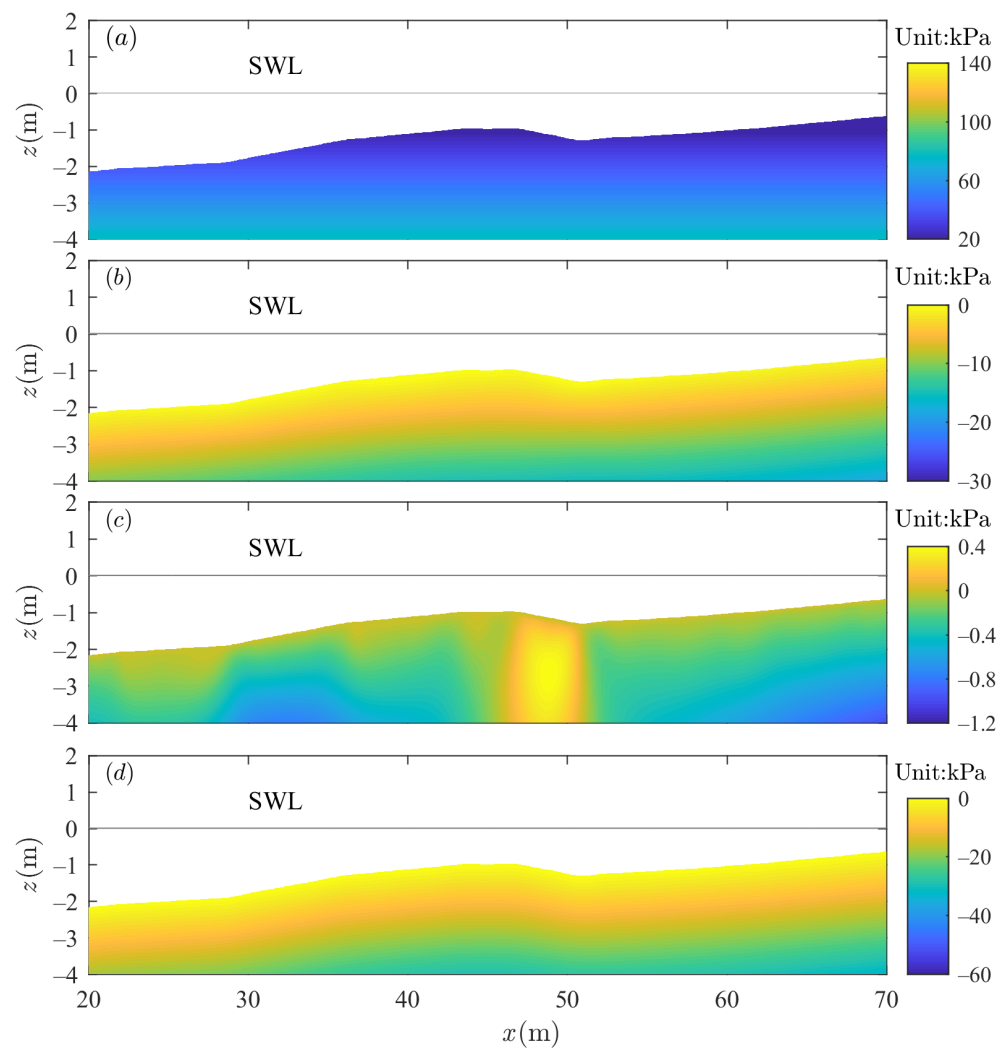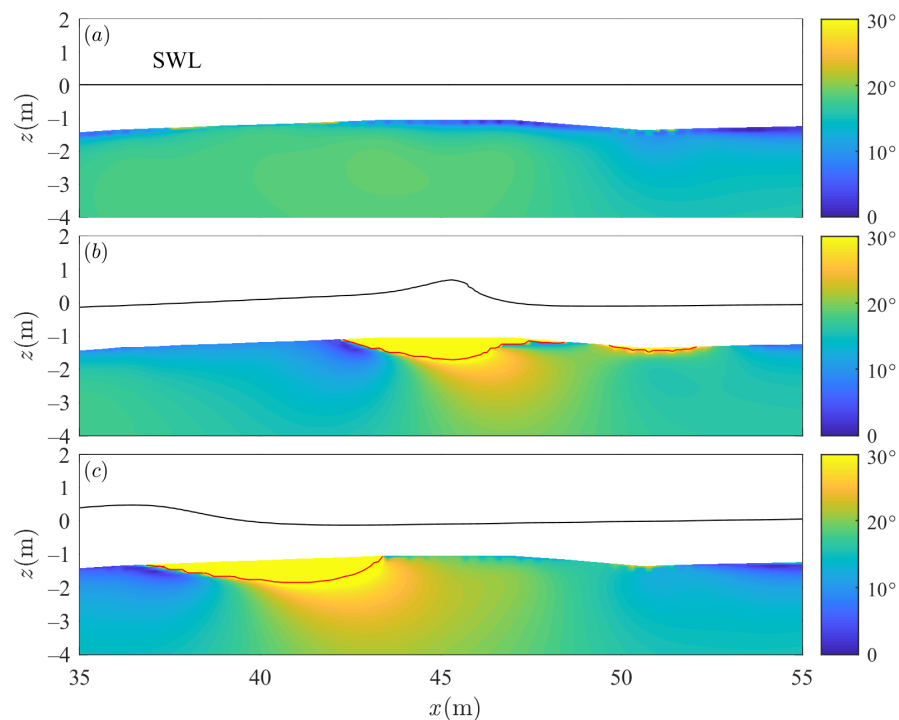


**Figure 15.** The initial consolidation state of the seabed. (**a**) Pore pressure p distribution around sandbar, (**b**) horizontal effective stress $\tau_{xx}$ distribution around sandbar, (**c**) shear stress $\tau_{xz}$ distribution around sandbar, (**d**) vertical effective stress $\tau_{zz}$ distribution around sandbar. SWL represents still water level.

A common method for estimating the wave–induced shear failure in the seabed is the Mohr–Coulomb criterion. When the stress angle $\theta$ is more than or equal to the friction angle $\phi$ of sandy seabed, shear failure occurs:

$$\theta = \arcsin\left(\frac{\frac{\sigma_1' - \sigma_3'}{2}}{\frac{c}{\tan\phi} + \frac{\sigma_1' + \sigma_3'}{2}}\right) \geq \phi \tag{19}$$

where $c$ and $\phi$ are the cohesion and friction angle of the sandy seabed, respectively; $\sigma_1'$ and $\sigma_3'$ are the maximum and minimum principal effective stresses.

In this study, $c = 0$ and $\phi = 35°$ are applied for the sandbar soil in numerical computation. Figure 16 shows the distribution of stress angle $\theta$ at initial consolidation state, wave crest, and wave trough. In the consolidation state, the shear stress angle is less than 35°. This indicates that the sandbar is stable under the initial consolidation state. When the wave crest passes through the sandbar, the shear failure zone concentrates in the middle of the sandbar, ranging from $x = 42.1$ m to $x = 47$ m. The maximum shear failure depth reaches 0.7 m. Shear failure also occurs at the lateral turning point of the sandbar topography ($x = 49.7$–52.1 m). This may be due to the rigid transition of the seabed setup in the numerical model, which results in shear failure and a smoother connection between the sandbar and the seabed. When the wave trough propagates to the sandbar, the impact of wave on the distribution of stress angle at the front end of the sandbar is obvious, ranging from $x = 37$ m to $x = 43.3$ m. The maximum shear failure depth reaches 0.8 m. Compared to the wave crest moment, the range of shear failure around the sandbar is wider and the depth is deeper when the wave trough arrives. This may be due to wave energy dissipation caused by wave breaking when the wave crest arrives, which reduces the force exerted by the waves on the sandbar. Tong and Liu [51] also computed the stress angle distribution in a flat seabed with the wave and soil parameters supplied by Anderson et al. [11]. They concluded that shear failure would not occur in the seabed under this condition, which is contrary to our results. One possible explanation is that they neglected to restore the sandbar's topography and set a thinner seabed thickness.



**Figure 16.** Distribution of stress angle $\theta$ around the sandbar. (**a**) The initial consolidation status; (**b**) under the wave crest (at $t = 37.5$ s); (**c**) under the wave trough (at $t = 35.3$ s).

## 4. Conclusions

In this paper, based upon the RANS equations and *u–p* approximation theory, a two-dimensional numerical model, which is validated using available experiments, is established to analyze the dynamics response and stability of a sandbar seabed under the regular waves. Parametric studies are then launched to evaluate the impact of the wave parameters and soil properties on soil dynamics. The following conclusions can be reached:

1.  The vertical distribution of the maximum vertical effective stress in the sandbar differs from that in the flat seabed, which is inferred to be affected by wave shoaling. The vertical effective stress inside the sandbar decreases rapidly and then grows gradually along the soil depth.
2.  The soil response in the sandbar is affected by wave conditions. In addition to the vertical displacement of soil particles, the soil response in the sandbar increases as wave period and wave height increase. The horizontal displacement of soil particles is not affected by the wave conditions. In addition, the soil response in the sandbar is more sensitive to the change in wave period than that of wave height. It is worth noting that the impact of wave period on the vertical distribution of shear stress in the sandbar is different from that on the flat seabed.
3.  Soil properties also play a crucial role in soil response around the sandbar. The soil response increases as the soil permeability coefficient grows except for the vertical displacement of soil particles. With the increase in soil permeability coefficient, the vertical displacement of shallow soil particles declines, while the vertical displacement of deeper soil particles is unaffected. With increasing soil shear modulus, the pore pressure, soil particle displacement, and horizontal effective stress decrease, while the shear stress and vertical effective stress increase first and then decrease as soil depth increases. Additionally, when initial soil saturation increases, the pore pressure, soil particle horizontal displacement, and horizontal effective stress increase, and soil particle vertical displacement slightly decreases. The vertical effective stress decreases first and then increases as soil depth increases. As the soil saturation grows, the shear stress inside the seabed soil increases and then decreases. Unlike the flat seabed, the vertical distribution of the vertical effective stress inside the sandbar increases as soil permeability increases, declines first, and then increases as soil saturation increases.
4.  The sandbar soil shear failure potential is discussed according to the Mohr–Coulomb criterion. The sandbar undergoes shear failure during the wave propagation. The range of shear failure around the sandbar is wider and the depth is deeper when the wave trough arrives.

One of the limitations of the current study is that only the impact of wave action on the soil response around the sandbar has been considered. In natural marine environments, wave propagation is usually accompanied by currents. The presence of currents may affect the shear stress on the seabed surface. For future work, further consideration will be given to the bed shear stress around the sandbar under the combined effect of wave and current, which may be useful for the understanding of the stability of the sandbar.

**Author Contributions:** Conceptualization, L.T.; methodology, N.C.; software, N.C.; validation, N.C. and L.T.; formal analysis, N.C. and Y.G.; investigation, N.C.; writing—original draft preparation, N.C., L.T., Y.G., B.L. and Z.Z.; writing—review and editing, J.Z.; visualization, N.C. and L.T.; supervision, L.T., J.Z. and Y.G.; project administration, L.T.; funding acquisition, L.T. All authors have read and agreed to the published version of the manuscript.

**Institutional Review Board Statement:** Not applicable.

**Informed Consent Statement:** Not applicable.

**Data Availability Statement:** The data presented in this study are available on request from the corresponding author. The data are not publicly available due to the policies and confidentiality agreements adhered to by the project.

**Conflicts of Interest:** Authors Bo Liu and Zhipeng Zhou were employed by the company China Power Engineering Consulting Group Co., Ltd. The remaining authors declare that the research was conducted in the absence of any commercial or financial relationships that could be construed as a potential conflict of interest.

## References

1.  Reguero, B.G.; Losada, I.J.; Méndez, F.J. A Recent Increase in Global Wave Power as a Consequence of Oceanic Warming. *Nat. Commun.* **2019**, *10*, 205. [CrossRef] [PubMed]
2.  Shi, J.; Feng, X.B.; Toumi, R.; Zhang, C.; Hodges, K.I.; Tao, A.F.; Zhang, W.; Zheng, J.H. Global Increase in Tropical Cyclone Ocean Surface Waves. *Nat. Commun.* **2024**, *15*, 174. [CrossRef] [PubMed]
3.  Gallagher, E.L.; Elgar, S.; Guza, R.T. Observations of sand bar evolution on a natural beach. *J. Geophys. Res. Ocean.* **1998**, *103*, 3203–3215. [CrossRef]
4.  Anderson, D.L.; Bak, A.S.; Cohn, N.; Brodie, K.L.; Johnson, B.B.; Dickhudt, P. The Impact of Inherited Morphology on Sandbar Migration During Mild Wave Seasons. *Geophys. Res. Lett.* **2023**, *50*, e2022GL101219. [CrossRef]
5.  Yu, J.; Mei, C.C. Formation of Sand Bars under Surface Waves. *J. Fluid Mech.* **2000**, *416*, 315–348. [CrossRef]
6.  Liu, P.L.-F.; Chan, I.C. On Long-wave Propagation over a Fluid-mud Seabed. *J. Fluid Mech.* **2007**, *579*, 467–480. [CrossRef]
7.  Liu, Z.; Jeng, D.-S.; Chan, A.H.C.; Luan, M. Wave-induced Progressive Liquefaction in a Poro-elastoplastic Seabed: A Two-layered Model. *Int. J. Numer. Anal. Methods Geomech.* **2009**, *33*, 591–610. [CrossRef]
8.  Liu, X.L.; Chai, N.; Zhao, H.Y.; Jeng, D.-S.; Zhou, J. Numerical Investigation into Wave-induced Progressive Liquefaction Based on a Two-layer Viscous Fluid System. *Comput. Geotech.* **2023**, *159*, 105447. [CrossRef]
9.  Baldock, T.E.; Baird, A.J.; Horn, D.P.; Mason, T. Measurements and Modeling of Swash-induced Pressure Gradients in the Surface Layers of a Sand Beach. *J. Geophys. Res. Ocean.* **2001**, *106*, 2653–2666. [CrossRef]
10. Mason, H.B.; Yeh, H. Sediment Liquefaction: A Pore-water Pressure Gradient Viewpoint. *Bull. Seismol. Soc. Am.* **2006**, *106*, 1908–1913. [CrossRef]
11. Anderson, D.; Cox, D.; Mieras, R.; Puleo, J.A.; Hsu, T.-J. Observations of Wave-induced Pore Pressure Gradients and Bed Level Response on a Surf Zone Sandbar. *J. Geophys. Res. Ocean.* **2017**, *122*, 5169–5193. [CrossRef]
12. Tong, L.; Zhang, J.; Zhao, J.; Zheng, J.; Guo, Y. Modelling Study of Wave Damping over a Sandy and a Silty Bed. *Coast. Eng.* **2020**, *161*, 103756. [CrossRef]
13. Yamamoto, T. Wave-induced Pore Pressures and Effective Stresses in Inhomogeneous Seabed Foundations. *Ocean Eng.* **1981**, *8*, 1–16. [CrossRef]
14. Jeng, D.-S.; Rahman, M.S. Effective Stresses in a Porous Seabed of Finite Thickness: Inertia Effects. *Can. Geotech. J.* **2000**, *37*, 1383–1392. [CrossRef]
15. Jeng, D.-S.; Cha, D.H. Effects of Dynamic Soil Behavior and Wave Non-linearity on the Wave-induced Pore Pressure and Effective Stresses in Porous Seabed. *Ocean Eng.* **2003**, *30*, 2065–2089. [CrossRef]
16. Ren, Y.; Xu, X.; Zhao, T.; Wang, X. The Initial Wave Induced Failure of Silty Seabed: Liquefaction or Shear Failure. *Ocean Eng.* **2020**, *200*, 106990. [CrossRef]
17. King, C.A.; Williams, W.W. The Formation and Movement of Sand Bars by Wave Action. *Geogr. J.* **1949**, *113*, 70. [CrossRef]
18. Benjamin, T.B.; Boczar-Karakiewicz, B.; Pritchard, W.G. Reflection of Water Waves in a Channel with Corrugated Bed. *J. Fluid Mech.* **1987**, *185*, 249–274. [CrossRef]
19. Reniers, A.J.; Thornton, E.B.; Stanton, T.; Roelvink, J.A. Vertical Flow Structure during Sandy Duck: Observations and Modeling. *Coast. Eng.* **2004**, *51*, 237–260. [CrossRef]
20. Cohn, N.; Ruggiero, P.; Oritz, J.; Walstra, D.J. Investigating the Role of Complex Sandbar Morphology on Nearshore Hydrodynamics. *J. Coast. Res.* **2014**, *70*, 53–58. [CrossRef]
21. Chiapponi, L.; Cobos, M.; Losada, M.A.; Longo, S. Cross-shore Variability and Vorticity Dynamics during Wave Breaking on a Fixed Bar. *Coast. Eng.* **2017**, *127*, 119–133. [CrossRef]
22. Van der, A.D.A.; Van der Zanden, J.; O'Donoghue, T.; Hurther, D.; Cáceres, I.; McLelland, S.J.; Ribberink, J.S. Large-scale Laboratory Study of Breaking Wave Hydrodynamics over a Fixed Bar. *J. Geophys. Res. Ocean.* **2017**, *122*, 3287–3310. [CrossRef]
23. Van der Zanden, J.; Van der, A.D.A.; Cáceres, I.; Hurther, D.; McLelland, S.J.; Ribberink, J.S.; O'Donoghue, T. Near-bed Turbulent Kinetic Energy Budget under a Large-scale Plunging Breaking Wave over a Fixed Bar. *J. Geophys. Res. Ocean.* **2018**, *123*, 1429–1456. [CrossRef]
24. Mulligan, R.P.; Gomes, E.R.; Miselis, J.L.; McNinch, J.E. Non-hydrostatic Numerical Modelling of Nearshore Wave Transformation over Shore-oblique Sandbars. *Estuar. Coast. Shelf Sci.* **2019**, *219*, 151–160. [CrossRef]
25. Larsen, B.E.; Van der, A.D.A.; Van der Zanden, J.; Ruessink, G.; Fuhrman, G.R. Stabilized RANS Simulation of Surf Zone Kinematics and Boundary Layer Processes beneath Large-scale Plunging Waves over a Breaker Bar. *Ocean Model.* **2020**, *155*, 101705. [CrossRef]

26. Wang, J.; Wang, T.; Xing, F.; Wu, H.; Jia, J.; Yang, Z.; Wang, Y. Internal Waves Triggered by River Mouth Shoals in the Yangtze River Estuary. *Ocean Eng.* **2020**, *214*, 107828. [CrossRef]

27. Fang, H.Q.; Tang, L.; Lin, P.Z. Bragg scattering of nonlinear surface waves by sinusoidal sandbars. *J. Fluid Mech.* **2024**, *979*, A13. [CrossRef]

28. Gao, J.L.; Ma, X.Z.; Dong, G.H.; Chen, H.Z.; Liu, Q.; Zang, J. Investigation on the effects of Bragg reflection on harbor oscillations. *Coast. Eng.* **2021**, *170*, 103977. [CrossRef]

29. Gao, J.L.; Shi, H.B.; Zang, J.; Liu, Y.Y. Mechanism analysis on the mitigation of harbor resonance by periodic undulating topography. *Ocean Eng.* **2023**, *281*, 114923. [CrossRef]

30. Gao, J.L.; Hou, L.H.; Liu, Y.Y.; Shi, H.B. Influences of bragg reflection on harbor resonance triggered by irregular wave groups. *Ocean Eng.* **2024**, *305*, 117941. [CrossRef]

31. Liu, P.L.-F.; Park, Y.S.; Lara, J.L. Long-wave-induced flows in an unsaturated permeable seabed. *J. Fluid Mech.* **2007**, *586*, 323–345. [CrossRef]

32. Carraro, T.; Goll, C.; Marciniak-Czochra, A.; Mikelić, A. Pressure jump interface law for the Stokes–Darcy coupling: Confirmation by direct numerical simulations. *J. Fluid Mech.* **2013**, *732*, 510–536. [CrossRef]

33. Biot, M.A. General theory of three-dimensional consolidation. *J. Appl. Phys.* **1941**, *12*, 155–164. [CrossRef]

34. Jeng, D.-S. Wave-induced sea floor dynamics. *Appl. Mech. Rev.* **2003**, *56*, 407–429. [CrossRef]

35. Yamamoto, T.; Koning, H.L.; Sellmejjer, H.; Hijum, H.L. On the response of a poro-elastic bed to water waves. *J. Fluid Mech.* **1978**, *87*, 193–206. [CrossRef]

36. Jeng, D.-S.; Hsu, J.R.C. Wave-induced soil response in a nearly saturated sea-bed of finite thickness. *Géotechnique* **1996**, *46*, 427–440. [CrossRef]

37. Jeng, D.-S.; Seymour, B.R. Response in seabed of finite depth with variable permeability. *J. Geotech. Geoenviron. Eng.* **1997**, *123*, 9–19. [CrossRef]

38. Xu, L.Y.; Chen, W.Y.; Zhao, K.; Cai, F.; Zhang, J.Z.; Chen, G.X.; Jeng, D.-S. Poro-elastic and Poro-elasto-plastic Modeling of Sandy Seabed under Wave Action. *Ocean Eng.* **2022**, *260*, 112002. [CrossRef]

39. Tong, L.L.; Zhang, J.S.; Chen, N.; Lin, X.F.; He, R.; Sun, L. Internal solitary wave-induced soil responses and its effects on seabed instability in the South China Sea. *Ocean Eng.* **2024**, *310*, 118697. [CrossRef]

40. Zhao, H.Y.; Liang, Z.D.; Jeng, D.-S.; Zhu, J.F.; Guo, Z.; Chen, W.Y. Numerical investigation of dynamic soil response around a submerged rubble mound breakwater. *Ocean Eng.* **2018**, *156*, 406–423. [CrossRef]

41. Rafati, Y.; Hsu, T.J.; Elgar, S.; Raubenheimer, B.; Quataert, E.; Van Dongeren, A. Modeling the hydrodynamics and morphodynamics of sandbar migration events. *Coast. Eng.* **2021**, *166*, 103885. [CrossRef]

42. Patrick, M.; Chauchat, J.; Shafiei, H.; Almar, R.; Benshila, R.; Dumas, F.; Debreu, L. 3D wave-resolving simulation of sandbar migration. *Ocean Model.* **2022**, *180*, 102127.

43. Shtremel, M.; Saprykina, Y.; Ayat, B. The method for evaluating cross-shore migration of sand bar under the influence of nonlinear waves transformation. *Water* **2022**, *14*, 214. [CrossRef]

44. Grossmann, F.; Hurther, D.; van der Zanden, J.; Sánchez-Arcilla, A.; Alsina, J.M. Near-bed sediment transport processes during onshore bar migration in large-scale experiments: Comparison with offshore bar migration. *J. Geophys. Res. Ocean.* **2023**, *128*, e2022JC018998. [CrossRef]

45. Mieras, R.S.; Puleo, J.A.; Anderson, D.; Cox, D.T.; Hsu, T.J. Large-scale experimental observations of sheet flow on a sandbar under skewed-asymmetric waves. *J. Geophys. Res. Ocean.* **2017**, *122*, 5022–5045. [CrossRef]

46. Islam, M.S.; Suzuki, T.; Thilakarathne, S. Physical modeling of sandbar dynamics to correlate wave-induced pore pressure gradient, sediment concentration, and bed-level erosion. *Ocean Eng.* **2024**, *307*, 118161. [CrossRef]

47. Launder, B.E.; Spalding, D.B. The numerical computation of turbulent flows. *Comput. Methods Appl. Mech. Eng.* **1974**, *3*, 269–289. [CrossRef]

48. Lin, P.Z.; Liu, P.L.-F. Internal wave-maker for navier-stokes equations models. *J. Waterw. Port Coast. Ocean Eng.* **1999**, *125*, 207–215. [CrossRef]

49. Hirt, C.W.; Nichols, B.D. Volume of fluid (VOF) method for the dynamics of free boundaries. *J. Comput. Phys.* **1981**, *39*, 201–225. [CrossRef]

50. Zhang, J.S.; Zhang, Y.; Jeng, D.-S.; Liu, P.L.-F.; Zhang, C. Numerical simulation of wave–current interaction using a RANS solver. *Ocean Eng.* **2014**, *75*, 157–164. [CrossRef]

51. Tong, L.L.; Liu, P.L.-F. Transient Wave-induced Pore-water-pressure and Soil Responses in a Shallow Unsaturated Poroelastic Seabed. *J. Fluid Mech.* **2022**, *938*, A36. [CrossRef]

52. Wang, J.G.; Zhang, B.Y.; Nogami, T. Wave-induced seabed response analysis by radial point interpolation meshless method. *Ocean Eng.* **2004**, *31*, 21–42. [CrossRef]

53. Zhai, Y.Y.; He, R.; Zhao, J.L.; Zhang, J.S.; Jeng, D.-S.; Li, L. Physical model of wave-induced seabed response around trenched pipeline in sandy seabed. *Appl. Ocean Res.* **2018**, *75*, 37–52. [CrossRef]

54. Hsu, J.R.C.; Jeng, D.-S. Wave-induced soil response in an unsaturated anisotropic seabed of finite thickness. *Int. J. Numer. Anal. Methods Geomech.* **1994**, *18*, 785–807. [CrossRef]

55. Zhao, K.F.; Wang, Y.F.; Liu, P.L.-F. A guide for selecting periodic water wave theories—Le Méhauté (1976)'s graph revisited. *Coast. Eng.* **2024**, *188*, 104432. [CrossRef]

56.  Jeng, D.-S.; Lin, Y.S. Non-Linear Wave-Induced Response of Porous Seabed: A Finite Element Analysis. *Int. J. Numer. Anal. Methods Geomech.* **1997**, *21*, 15–42. [CrossRef]
57.  Madsen, O.S. Wave-induced pore pressures and effective stresses in a porous bed. *Géotechnique* **1978**, *28*, 377–393. [CrossRef]
58.  Ulker, M.B.C.; Rahman, M.S.; Jeng, D.-S. Wave-induced Response of Seabed: Various Formulations and Their Applicability. *Appl. Ocean Res.* **2009**, *31*, 12–24. [CrossRef]